Composite Electrode (LiNi 0.6 Mn 0.2 Co 0.2 O 2) Engineering for Thiophosphate Solid-State Batteries: Morphological Evolution and Electrochemical Properties

Patrice Perrenot, Pascale Bayle-Guillemaud, Claire Villevieille

Composite electrode ($LiNi_{0.6}Mn_{0.2}Co_{0.2}O_2$) engineering for thiophosphate solid-state batteries: morphological evolution and electrochemical properties

Patrice Perrenot[1], Pascale Bayle-Guillemaud[1], Claire Villevieille[2]**

1 Université Grenoble Alpes, CEA, 17 Avenue des Martyrs, 38054 Grenoble, France,

2 Univ. Grenoble Alpes, Univ. Savoie Mont Blanc, CNRS, Grenoble INP, LEPMI, 38000 Grenoble, France

Corresponding Author

* E-mail: pascale.bayle-guillemaud@cea.fr, claire.villevieille@grenoble-inp.fr

ABSTRACT

Solid-state batteries using thiophosphate electrolytes are believed to be the forthcoming solid electrolyte, but they suffer from several issues including also the engineering of the composite positive electrode. To date, the relationship between the morphology of the composite electrode and its electrochemical performance remains undetermined. By using Focused Ion Beam - Scanning Electron Microscopy (FIB-SEM) tomography, we investigated several electrode engineering of polycrystalline NMC 622 ($LiNi_{0.6}Mn_{0.2}Co_{0.2}O_2$) particles and amorphous Li_3PS_4 solid electrolyte. Based on the morphological analysis of the electronic and ionic networks, it is possible to determine that the electrochemical performance limitation in this cell emerges from the surface contact between the NMC and the LPS as the sintering of the solid electrolyte (SE) is far from optimal. Additionally, similar analyses are performed after the first charge shows that the fading of the electrochemical is linked to the morphological evolution in the composite cathode.

TOC GRAPHICS

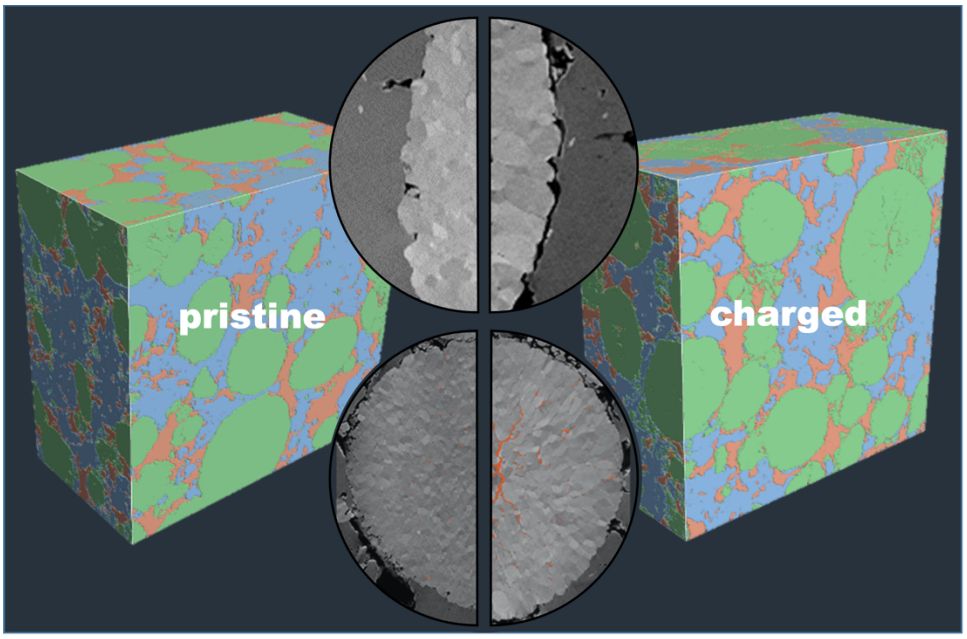
pristine
charged

In the coming years, solid-state batteries (SSB) will take a predominant position in the field of rechargeable battery[1–3]. However, such improvements will only be possible if one can control the several interfaces especially the one of the composite positive electrode between the solid electrolyte and the electroactive materials[4,5]. To achieve such goals, a fine understanding of both the chemistry and the morphology is required to lift the chemo-mechanical degradation. The chemical degradations are an important parameters to control[6–8] since they lower the electrochemical performance and increase the overall cell resistance during cycling. However, the chemical degradation is a well know process already reported in conventional Li-ion batteries and thus knowledge acquired on coating and protective layers can directly be applied to solid state batteries[9–14]. As an example, advanced coating made of Li-Nb-O drastically reduces the chemical degradation leading to an improvement of the electrochemical performance upon ageing[15,16]. The mechanical degradations are more difficult to tackle, since these issues are not really existing in conventional Li-ion batteries due to the wetting properties of the liquid electrolyte and of the porous nature of the composite electrode compared to the solid state one. Thus, the electroactive materials breathing[17] occurring during cycling might lead to additional irreversible degradation[18–22] that could be buffered depending on the Young modulus of the solid electrolyte and depending on the embedded properties of the electroactive material within the solid electrolyte matrix. As an example, the unit cell volume change of $LiNi_{0.6}Mn_{0.2}Co_{0.2}O_2$ (NMC 622) is reported to be 4.4 % at a 4.5 V vs Li^+/Li[23] as the lattice parameters will undergo anisotropic evolution[24,25]. The main morphological consequence arising from this volume change is the cracking of polycrystalline NMC along the

grain boundaries during cycling[25–28]. This effect has moderate consequences in a conventional lithium-ion battery as the liquid electrolyte adjust to those morphological changes but is problematic in the fixed nature of SSB. Moreover, the active material breathing will be transferred to the solid electrolyte that will subsequently need to adapt to the local change. Sulfide solid electrolyte have interesting mechanical properties with a Young moduli around 20 GPa[29] and generally able to manage little volume change, especially true when amorphous solid electrolyte are employed since the stress/strain cannot propagate along grains boundaries[30–32]. Additionally, one should pay attention to the pressure used for cycling which is independent from the one applied for the sintering of the solid electrolyte/composite electrode[33–35]. Indeed, when the sintering is properly performed in the solid electrolyte and on the composite electrode, there is no need of a strong pressure to be applied on the cell. However, the story is different when the cell stack is fully assembled and that the counter electrode needs to be properly "attached" to the separator which has a certain surface rugosity. Closing the cell just with the screws is not enough to maintain properly the contact between the negative electrode and the electrochemical stack, which turns into high polarization of the cells and poor electrochemical performance, mostly caused by poor contact (too high porosity and tortuosity). When high pressure is applied, then dendrites come faster hindering proper electrochemical cycling. Thus, an optimal pressure should be selected to ensure the deconvolution of the processes, meaning the one related to the sintering and the one related to the counter electrode/surface adhesion.

In this paper, we focus on the investigation of a composite electrode made of NMC622 and LPS solid electrolyte to propose a methodology monitoring the proper adhesion of the solid electrolyte to the electroactive material particles. NMC particles were selected for their high voltage properties being one of the most used positive electrodes nowadays with a particular round-shape morphology, whereas LPS solid electrolyte was selected based on its high ductility, easy synthesis, and low cost. We propose here an in-depth understanding of the room temperature sintering of composite positive electrode material is presented. The morphologies of the obtained composite electrode (made of LPS and NMC622) are monitored by FIB-SEM tomographies while the electrochemical performance are assessed by means of CCCV protocol (constant current/constant voltage). In order to compare the samples, a methodical image analysis approach is applied on all samples and metrics (tortuosity, developed surfaces, etc.) are correlated to electrochemical response (specific capacity, overpotential). Analysis after the first charge allows to track morphological evolution and identify phenomenon behind the specific capacity loss of the SSB.

To ensure a proper cycling, three main aspects should be considered, the electronic transport, the ionic transport, and the solid-state diffusion within the particles. The composite electrode should then be optimized to fulfil the two main criteria since the last one is more linked to the materials properties. To ensure a good electronic and ionic percolation, solid-state composite electrode should be sintered to avoid any porosity. This process results in the formation of both an electronic network, primarily composed of NMC (as no conductive carbon is introduced), and an ionic network, predominantly represented by LPS. As LPS is

significantly softer than NMC (ca. 20 GPa for LPS[29] and ca. 199 GPa for NMC 111[36]), the contact between LPS and NMC should be optimal. However, with the ratio used to maximize the energy density and to ensure good electronic percolation, NMC particle will be in contact with NMC particles, and it is believed that the NMC secondary particles will fracture along the grain boundaries of the primary particles under pressure by contact point between them. To assess this fracturation, we performed a preliminary investigation, where only NMC particles have been uniaxially pressed and infused with fluid resin.

The estimation of the developed surface presented in **Figure S1**(Supporting Information) is equivalent to the NMC surface over its volume (A_{NMC}/V_{cell}), later presented for tomographic volumes. The initial developed surface is ca. 0.66 μm^{-1} and increases with the applied pressure as expected by the secondary particle fracturation along the grain boundaries (**Figure S2**, Supporting Information). Indeed, NMC622 secondary particles are synthetized by co-precipitation method to obtain spherical shape consisting of the agglomeration of primary nano-particles. At only 127 MPa, the developed surface almost double from its initial state and at 255 MPa, it had almost tripled from 0.66 to 1.83 μm^{-1}. As such, the development of a large surface is not particularly detrimental for the electrochemical performance only if the broken pieces remain electronically and ionically connected. However, this should not be the case in solid-state system since the fracturation generally happens at the surface of the particle and propagates to the core. At the surface, contact between NMC and LPS is still good, but the solid electrolyte will not fill the void meaning that the path of Li-ion through NMC layers structure will lengthen. Those fractures will thus decrease the rate at which the battery could

be cycled and additionally disconnect the inner part of the particle leading to dead volume/weight.

Based on these results, we look at two different time for the shaping of the composite electrode at 255 MPa for 10 min and 15 h to optimize the sintering of LPS without damaging too much the NMC particles. In addition, from a previous study on the LPS morphology carried in our laboratory[37], we expect a longer sintering to slightly reduce the porosity as well as improves the contact between NMC and LPS. For sake of simplicity, we will refer to the two samples 255-10m and 255-15h respectively.

Prior to any investigation related to the microstructure of the composite electrode, we first perform some electrochemical tests to see the impact of the sintering properties on the composite electrode. The two composite electrodes were tested in half-cell (vs. InLi metal). By carefully investigating the electrochemical data, we can already hint about the chemical and mechanical degradation occurring inside the electrochemical cell that we tried to summarize in **Figure S3** (Supporting Information). As can be seen in **Figure S4** (Supporting Information), the specific capacity retention is not the same for both composite electrodes, and the sole difference between them is the way they were processed. The composite electrode compressed for a longer time is outperforming the cell compressed for only a short time. After 10 cycles, the composite 255-15h still delivers more than 100 mAh/g, whereas the 255-10m delivers less than 50 mAh/g. (**Figure S6**) In both cases, we can note a poor Coulombic efficiency (CE) during the first cycle being lower than 85% and 70% for 255-10m and 255-15h respectively. The difference between them is supposed to mostly come from the intimate contact between the

electroactive material and the solid electrolyte. Indeed, with higher compressed electrode, we assume to get greater surface contact between particles, and thus a greater chemical decomposition. Here, we believe that the decompositions observed in the first cycle are mostly dominated by the chemical degradation, as witnessed by the poor electrochemical stability windows of LPS solid electrolyte[37]. Looking now at the other cycles, the tendency for the Columbic efficiency is drastically different for both samples, i) for the 255-10m, the CE remains poor for several cycles indicating additional chemical decomposition within the cell whereas ii) for the 255-15h, the CE increase directly to reach 97-98% for the next 10 cycles, indicating that the decomposition processes are drastically reduced. This behavior is counter intuitive and cannot be solely explained by the chemical degradation, since if the chemical degradation was the main cause of fading, the cell with supposedly better contact would have the worse electrochemical signature which is not the case, indicating that the mechanical stability is also playing a key role in improving the overall electrochemical performance. Indeed, once the chemical decomposition is occurring in the cell, it leads to a polarization building up and increases the contribution of charge gathered through the potentiostatic step; however, if the decomposition is caused by mechanical fractures or particles being disconnected from the electronic/ionic network, then the potentiostatic step would not lead to gather additional charges. Following this discussion, we looked at the evolution of the curve's polarization upon cycling for both samples (**Figure S5**, Supporting information) to estimate the resistance building up within the cell. Upon delithiation of NMC particles (**Figure S5a**), the polarization is building up in both compressed electrodes, slightly more for the 255-

10m than for the 255-15h. For the latter, we can see a strong evolution between the first and the second cycle then a kind of small polarization after each cycle, whereas for the 255-10m, the evolution between the first and second cycle is less sharp, but the evolution between each cycle is more important. It shows that the chemical degradations are occurring cycle after cycle, but they are more marked for the less compressed electrode, as already seeing by the CE. Again, this result is counterintuitive since in theory, the better the contact between the materials, the more chemical degradation, showing again that other processes than chemical ones are playing a role. Looking now at the current evolution during the potentiostatic step (**Figure S7**, Supporting information), the behaviour is different between the two composite electrodes. As can be seen for the 255-10m (**Figure S7a**), we can see that the current during the potenstiostatic step is always the same, with no evolution during cycling. This is rather surprising since the specific charge decreases during cycling and polarization increases, in theory, the potentiostatic step should be yielding a growing number of charges. Noentheless, this may not be the case if these charges are inaccessible due to mechanical fractures and reduced contact between the electroactive material and the solid electrolyte. For the 255-15h (**Figure S7b**), we can see that the current is less and less important cycle after cycle, which is indicating that the cell is also suffering some mechanical and chemical issues.

Based on the previous analyses of the electrochemical data, we believe that both chemical and mechanical issues are playing a role, the chemical one being the most important during the first cycle, whereas the mechanical one seems to be playing an important for the other cycles. Once the mechanical ones are playing a role, the charges cannot be accessible

because they are not anymore connected to the electronic/ionic network. We thus conducted a full investigation relying on FIB-SEM tomography to understand the role of the microstructure in the composite electrodes as a function of the sintering.

Tomographic volumes have been acquired for the two pristine composite electrodes. Their following 3D reconstructions are displayed in **Figure 1**. Representative Elementary Volume (REV) are obtained on each phase for every tomography and plots for each phase are presented in **Figure S8** (Supporting Information).

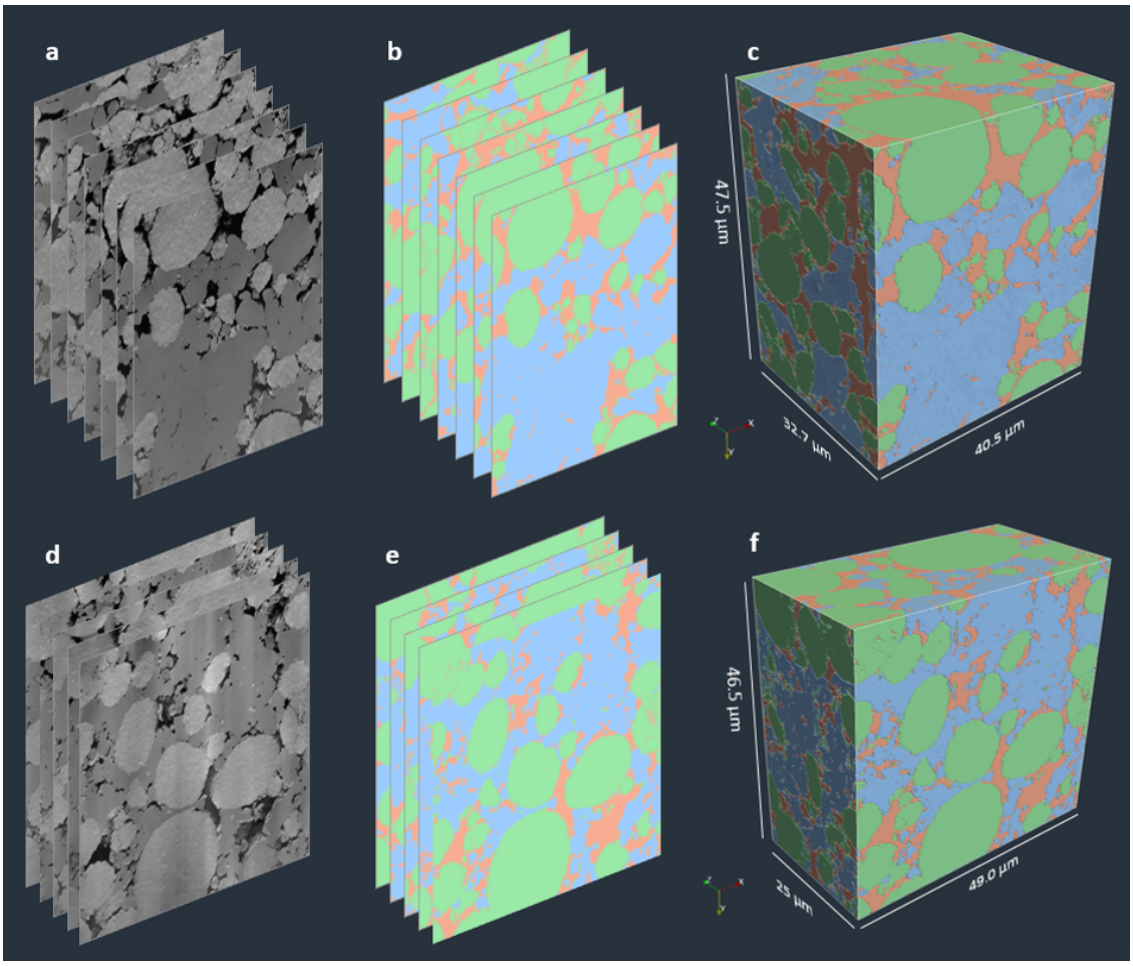

Figure 1: Composite electrode pressed at 255 MPa for a) – c) 10 min and d) – f) 15h. a), d) Secondary electrons images, b), e) segmented images and c), f) 3D reconstruction with NMC 622 in green, LPS in blue and porosity in orange.

Based on the data processing, we can extract several parameters divided into three categories: the first category will report general quantification of volume fraction. The second will report the description of the ionic network, i.e. the LPS. The third category will report the electronic network, i.e. the NMC. All those parameters are summarized in **Table 1**.

Metrics	Targeted	255 MPa

			10 min	15h	15h 1st charge
Volume fraction (%)	NMC	51	45.9	44.4	51.9
	LPS	49	33.7	38.6	29.8
	Porosity	/	20.2	16.7	18.1
	Unmarked	/	0.2	0.3	0.2
	NMC:LPS ratio	51:49	58:42	53:47	64:36
Ionic network	$\tau_{+/-y}$ tortuosity LPS	/	1.52	1.29	1.31
	Average local thickness (µm)	/	1.76	1.40	1.37
	Std dev. local thickness (µm)	/	0.88	0.72	0.80
Electronic network	$\%connected_{NMC}$	/	98.1	97.3	98.3
	A_{CAM}/V_{cell} (μm^{-1})	/	0.79	0.80	1.05
	$\%coverage_{NMC}$	/	25%	76%	42%

Table 1 . Summary of all the results extracted from tomographies. Composite electrode made with 70:30 wt.% NMC622:LPS ratio. Conversion to weight percentage to volume fraction are made using the density ρ_{LPS} = 1.88 g/cm^{3}and ρ_{NMC} = 4.6 g/cm^3.

As expected, the densification is always critical, and porosity should be reduced to a minimum to avoid electronic/ionic transport hindrance. In both composites, we found significant amount of porosity, 20.2 vol.% for the 255-10m and 16.7 vol.% for the 255-15h, as showed in **Figure S9**. As expected, a longer sintering reduces the amount of porosity in the

composite cathode. Additional issue with the porosity is their location inside the sample, and the connection between them. Located at the surface of the active materials would mean at best, a drastic hindrance of the transport and a high polarisation (poor interfacial contact), at worse, a full disconnection of the particle. Connected porosity within the sample could lead to a fragile mechanical ability (possible fracture along the pellet). Here, most of the porosity in the two samples are interconnected (98.1% and 97.3% for the 255-10m and the 255-15h respectively).

Two additional metrics can be used to characterize the ionic network i) the geometric tortuosity that describes the mean length from every path possible in the composite electrode from the current collector toward the separator, and, ii) the local thickness that describes the diameter of those paths (**Table 1**). The local thickness distribution is shown in **Figure S10** (Supporting Information). It can be seen that the average local thickness is slightly greater for the 255-10m than for the 255-15h with 1.76 μm and 1.40 μm respectively meaning that the sample pressed longer has more randomly distributed pores that decreases the local thickness. Despite the smaller local thickness, the tortuosity along the sintering axis (and lithium-ion transport paths) is smaller for the 255-15h than for the 255-10m with 1.29 and 1.52 respectively. It means that the transport is less hindered in the 255-15h despite the smaller Li-ion channel observed by local thickness measurement. Those results were coupled to DC polarization measurements as can be seen in **Figure S11** (for the electronic conductivity), **Figure S12** (for the ionic conductivity) and **Table S1**. As can be seen, both composite electrodes have roughly the same electronic conductivities, which is logical since in both cases we have

the same ratio of NMC particles and no conductive agent. For the ionic pathway, we can see a clear difference with less tortuosity and better effective ionic conductivity, as expected by the coverage of NMC622 particles by LPS in the more compressed electrode. Those results show that our methodology can be used on top of electrochemical performance to assess the electronic/ionic pathway. Based on these results, the electrochemical performance should be better for the sample with the lowest tortuosity (the one compressed the most, i.e. 15 h, which is the case). The local thickness could have an impact for fast charging but, as the solid electrolyte have a poor ionic conductivity to ensure fast charging, this parameter is less relevant.

Another parameter that needs to be considered is the electronic network within the composite electrode. In general, conductive agents are used to improve the electronic percolation in the composite electrode. However, in the present case of the fundamental understanding of the microstructure within the composite electrode and since long-term cycling nor fast charging is the scope of this manuscript, we decided to assess the electronic transport of the NMC particles only. Moreover, as the carbon additives are promoting interfacial reactions and enhance the electrolyte decomposition[38–40], we decided to make our composite electrode free of carbon. Thus, the electronic connection is only ensured by the contact among NMC particles in 3D. In both samples, most of the NMC particles are connected with each other (98.1 % and 97.3 % for the 255-10m and the 255-15h respectively). The small remaining fraction of unconnected NMC is generally linked to primary particles that fractured during the electrode preparation as they are entirely covered by LPS.

Another important parameter to assess is the surface coverage of the NMC particles, since the surface of the NMC (A_{NMC}) will be the site of lithium transfer reaction. We believe that the NMC particles are not serving for ionic pathway, since the LPS ionic conductivity is higher than the one of NMC particles. Each particle of NMC is either exposed to LPS ($A_{NMC\ active}$) or to the porosity ($A_{NMC\ inactive}$). Thus, the coverage of NMC could be deduced by:

$$\%coverage_{NMC} = \frac{A_{NMC\ active}}{A_{NMC}} \times 100 \qquad (1)$$

One can see a drastic change at the interface between the NMC and the SE (see **Table 1**) only 25% of the NMC surface is in contact with LPS in the 255-10m sample while it increases to 76% for the 255-15h. Based on this result, the 255-15h should outperform the 255-10m in term of electrochemical performance as seen in **Figure S4** (Supporting Information).

Their respective electrochemical response is given in **Figure S13** (Supporting Information). Compared to the delithiation in liquid electrolyte cell, the solid-state cells are more polarized (ca. 0.1 V) indicating a higher resistance. Both solid-state batteries show acceptable performance as can be seen in **Figure S4**.

To understand the role of the microstructure during cycling, the sample 255-15h was investigated after the 1st charge (3D analysis), the 1st discharge and after 11 cycles (2D analyses). For the end of the first charge of 255-15h, the REV plot shown on **Figure S14 (**Supporting Information) confirms the representativeness of the three phases. The reconstruction is shown in **Figure 2** and additional images comparing the pristine sample and end of charge sample can be found in **Figure S15** (Supporting Information).

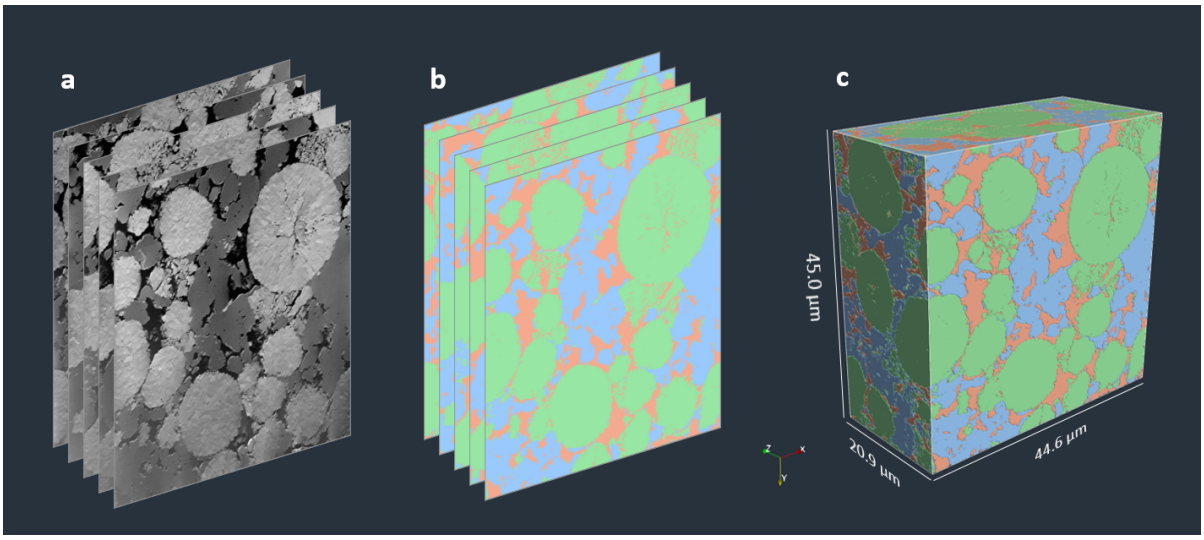

Figure 2. Composite electrode pressed at 255 MPa for 15h after the first charge. a) Secondary electrons images, b) segmented images and c) 3D reconstruction with NMC 622 in green, LPS in blue and porosity in orange

During delithiation, NMC622 undergoes some structural changes, especially an overall volume shrinkage with a large c lattice increase generating distortion on the crystal structure. It leads to inner fracturation of NMC secondary particles (**Figure S15** c & d) as it is discussed further in this section. The shrinkage of NMC volume (ca. 4%[23]) leads to 1.4% increase in porosity at the end of charge which is more or less logical based on the volume fraction of NMC used in the composite electrode (**Table 1**). The small difference between the theoretical volume change and the observed volume change could be explained by i) the local elasticity of LPS (Young modulus), and/or ii) the thick LPS separator (ca. 500 µm) acting as a spring elastically absorbing the deformation and/or iii) the InLi counter electrode expansion[41]. However, it is hard to discriminate one from the others as FIB-SEM tomography has a narrow

field of view compared to X-Ray Computed Tomography. Nevertheless, we demonstrated something similar with Sn negative electrode cycled with LPS. We believed that working hypothesis i) and ii) are playing a key role here[42].

Looking at the ionic network, the local thickness shows the same trends as the pristine sample but slightly more spread to smaller and bigger thicknesses (**Figure S16**, Supporting Information). The tortuosity remains equivalent to the pristine state showing that the electrochemical activity of NMC is not detrimental to the composite electrode integrity if the sample suffer only ca. 4% volume expansion.

Concerning the electronic network, the NMC connection is similar before and after the first charge. However, a higher surface of NMC (A_{NMC}/V_{cell}) is found on the sample after the first charge going from 0.80 to 1.05 μm^{-1}. Even if the volume fraction of NMC is different between the two tomographies (44.4 vol% to 51.9 vol% for before and after the charge respectively), the difference remains significant. Indeed, even when the surface of NMC is normalize to its volume fraction (A_{NMC}/V_{NMC}), the ratio still rises from 1.80 to 2.03 μm^{-1} before and after the first charge respectively. This observation could be explained by the NMC fracturing occurring during cycling[26,43]. Indeed, charged NMC particles show cracks within the secondary particle (**Figure 3**) coming from the change in the lattice parameters caused by the delithiation.

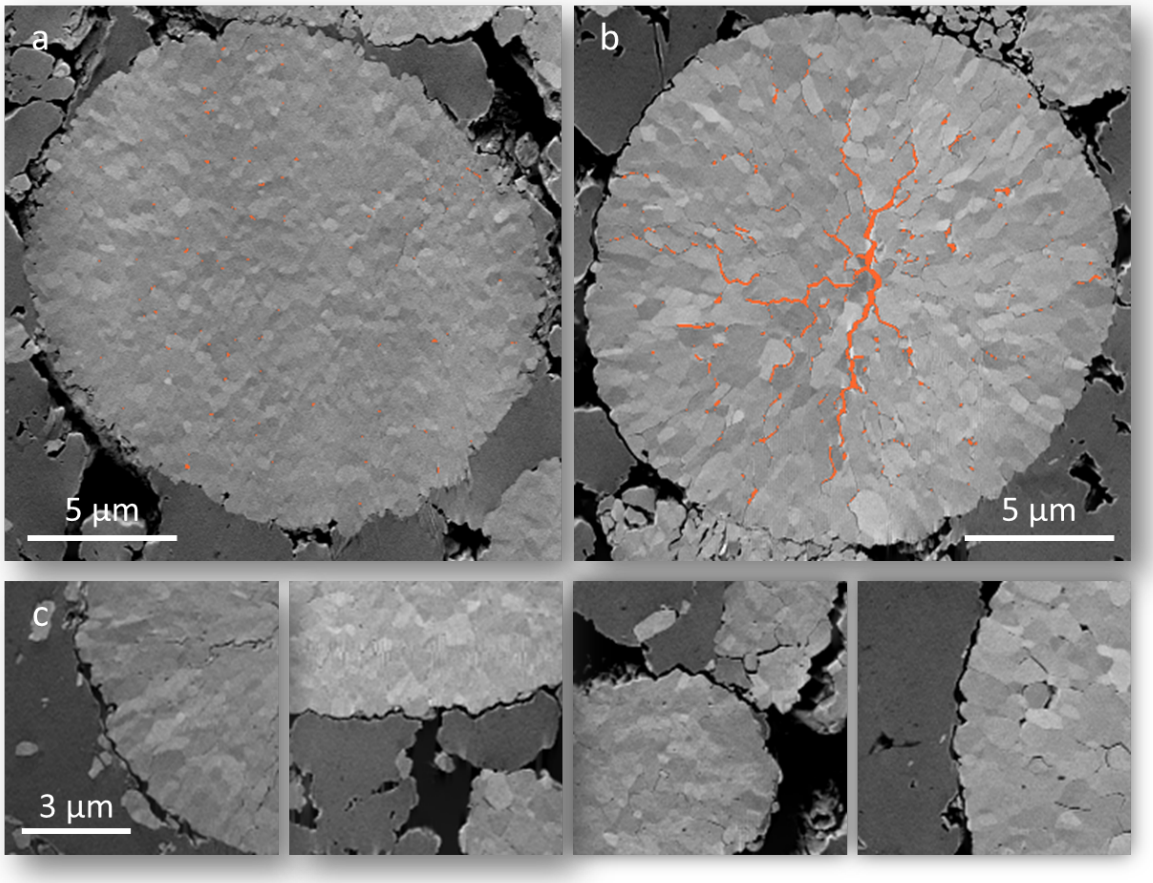

Figure 3. NMC in the composite cathode (secondary electrons image) sintered 15h at 255 MPa in a) pristine state and b) after the 1st charge extracted from the FIB-SEM stacks with the NMC in light grey, LPS in dark grey and porosity in black. The inner porosity is highlighted in orange. c) imprint of the NMC on the LPS underlying the NMC volume change, secondary electrons images extracted from the FIB-SEM stack in the charge state.

The NMC inner porosity on the pristine state is estimated to ca. 1.3 % of the overall porosity while it increases to ca. 2.5 % in the charge state, a value that doubles in only one charge. However, since we demonstrated that the composite electrode is somehow breathing during charge and since the electrolyte is having a certain Young modulus, we also investigate

the composite electrode after one full cycle, i.e. at the end of the lithiation of NMC particles. When comparing the sample at the end of charge (**Figure 3** and **Figure S15c** & **d**) to the one collected at the end of the discharge (**Figure 4**), it can be seen that a fraction of the inner NMC porosity is partially recovered as some fracture seems to "closed up" (to a certain extent) and some clearly remaining, hindering the Li-ion diffusion within the particles. Additionally, it can be seen in **Figure 4** that at the interface between LPS and NMC622, the NMC622 particles left an imprint on the LPS matrix, very similar to the one reported in **Figure 3c**. This means a gap is generated at the interface between NMC and LPS that will block the electronic/ionic transport; consequently, impacting the electrochemical performance (as stated above already). This result show that the mechanical processes are playing a key role in decreasing the electrochemical performance of the cell (as discussed already at the beginning of this paper).

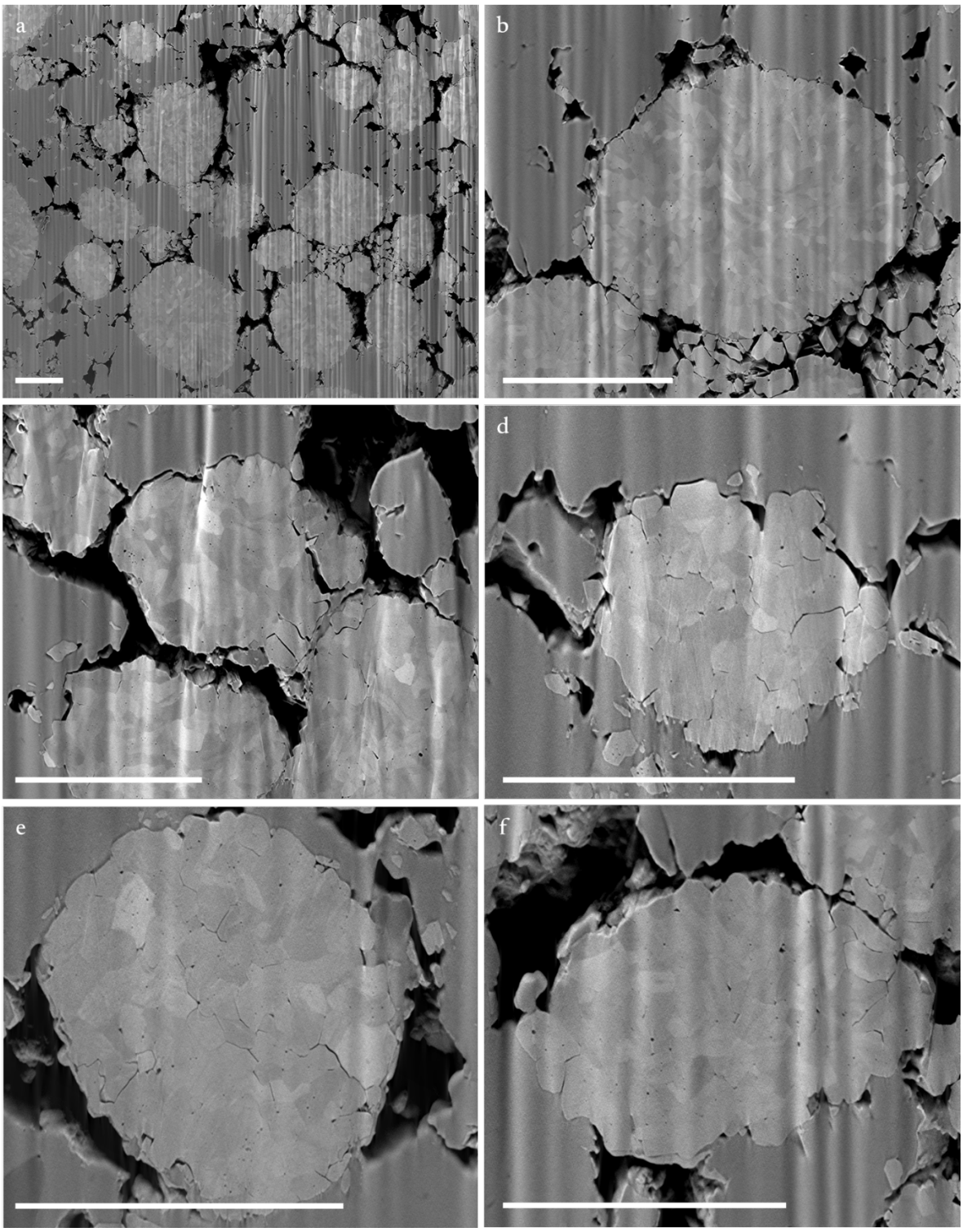

Figure 4. a) Secondary electrons image of the overall cross-section of composite electrode (255-15h) after 1 cycle (discharge) and b), to f) close-ups. The scale bars represent 10 μm.

Pursuing our investigation, we checked the microstructure evolution of the composite electrode after 11 cycles. As can be seen in **Figure 5**, there are still fracture inside the NMC particles that are not closing despite the successive charge/discharge process. It indicates that after a certain number of cycles, the mechanical fractures will lead to lower the electrochemical performance (as seen, especially for the poorly sintered composite electrode 255-10m) due to the Li-ion transport hindrance within the particles but also due to the gap of couple of nm (NMC imprint) let inside the LPS matrix, hindering the electronic and ionic transport.

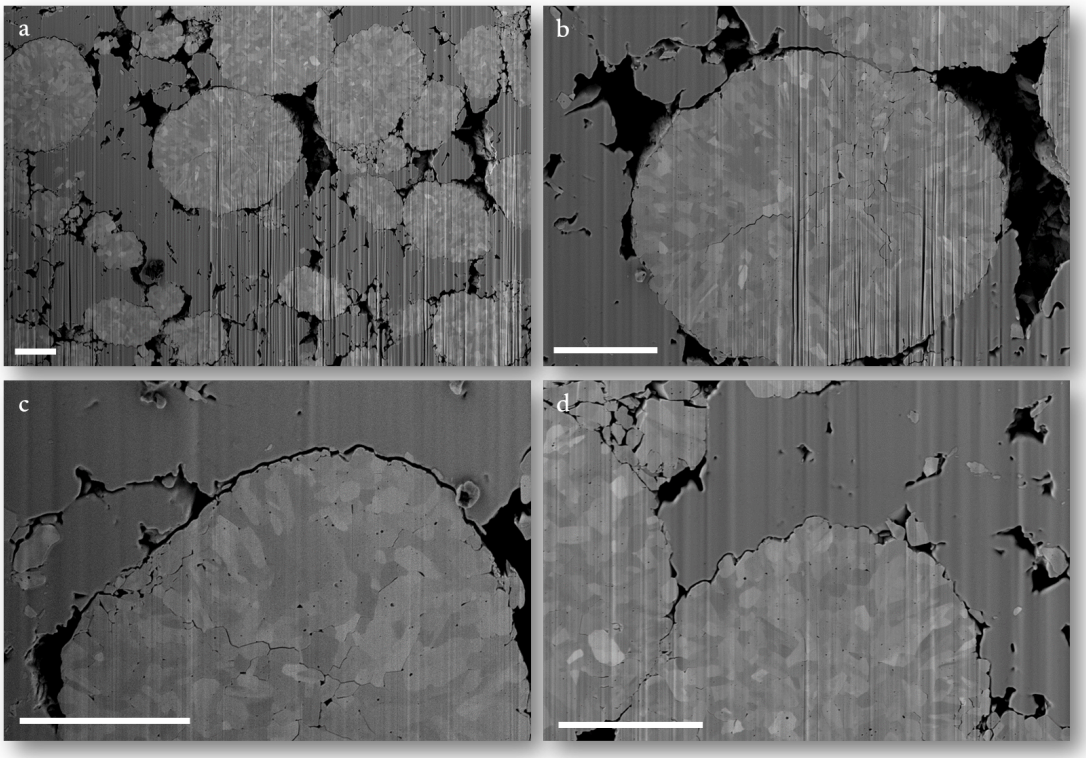

Figure 5. a) Secondary electrons image of the overall cross-section of the composite 255 MPa-15 h electrode after 11 cycles and b), c), d) close-ups. The scale bars represent 4 μm.

This evolution might be even more detrimental if one considered that hundreds of charges will be performed in commercial systems leading to more fractures created. Additionally, if the cracking happens close to the surface of the NMC particle, it could generate additional dead particles that will be either disconnected from the electronic/ionic network or from both. This cracking induced by shrinkage opens up NMC surfaces to the porosity yielding to a decrease on the coverage by LPS. This phenomenon is clearly visible on NMC particles that kept their integrity (**Figure 3a,b & Figure 5**), but it could happen to any particle that participates to the electrochemical processes. As the solid electrolyte would not be able to accommodate to the internal NMC fracturation imposed by the electrochemical activities, it will be detrimental for the specific capacity of the cell. In addition, when comparing the developed surface of NMC obtained in the first estimation (c.a. 1.8 μm^{-1} at 255 MPa) to the surfaces obtained from the tomography in the pristine state (c.a. 0.8 μm^{-1} at 255 MPa), it can be seen that LPS act as a buffer that mitigate the NMC fractures.

Finally, the percentage of coverage of the NMC by LPS decreases drastically after one single charge to 42% as expected from NMC particles shrinkage. This volume change leaves a visible imprint of the NMC on the LPS and creates a gap of few hundreds of nm between the active material and the electrolyte (**Figure 3**c) showing again the difficulty to control properly the solid/solid interface, despite a favorable Young modulus from LPS.

In this paper, the evolution of the microstructure in composite positive electrode made with solid electrolyte LPS and NMC622 was conducted. We first demonstrated that the morphology

of the polycrystalline NMC particles is not adapted for composite electrode for solid-state batteries, as the particles start to fracture under pressure. Nonetheless, it has been shown that the NMC fracturation is mitigated by the addition of soft material like LPS. LPS acts as a buffer between the secondary NMC particle by avoiding direct contact points and part of the pressure is redistributed to sinter the SE. Ionic and electronic conductive networks within the composite are impacted by porosity. It was found that most of NMC are electronically connected to the current collector at 255 MPa (98.1 %, 97.3 % and 98.3 for the 10min, 15h pristine and 15h after the first charge respectively) whereas it was established that a longer sintering time slightly decreases porosity and subsequently decreases geometric tortuosity, improving ionic transport. In addition, longer sintering time promotes an optimized contact between LPS and NMC without increasing the sintering pressure which ultimately would degrade even more NMC's morphology. We identify that the better cycling of the sample sintered 15h originates from the more intimate connection between NMC and LPS despite showing first an enhanced chemical decomposition. Unfortunately, after the first charge, NMC shrinkage leads to decohesion of the active material and the solid electrolyte, leading to low cycling ability.

Supporting Information

Figure S1: SEM images of NMC622 as a function of pressure applied; Figure S2: SEM images of NMC622 particles; Figure S3: Scheme explaining the difference between mechanical and electrochemical degradation; Figure S4-S7: Electrochemical data of NMC622 cycled vs. Li metal counter electrode; Figure S8: Representative elementary volume of NMC622 at pristine state; Figure S9: 3D tomograms showing the composite electrode; Figure S10: local thickness measurement: Figure S11-S12: DC polarization measurement; Figure S13: Electrochemical cycling data solid state batteries vs. liquid based batteries; Figure S14: Representative elementary volume of NMC622 after the first cycle; Figure S16: SEM images obtained along cycling of the composite electrode; Figure S16: local thickness after the first charge. Table S1: metrics extracted from DC polarization test. Supporting information contains also the materials & methods section.

ACKNOWLEDGMENT

We would also like to thank Thomas David for his insights and precious advice on FIB-SEM acquisition and data treatment. We are grateful to Magda Reuter for her support in electrochemical characterizations. Part of this work, carried out on the Platform of Nanocharacterization (PFNC), was supported by the “Recherche Technologique de Base”, program of the French National Research Agency (ANR) and by the ANR grant OpInSolid.

REFERENCES

1. Albertus, P., Babinec, S., Litzelman, S. & Newman, A. Status and challenges in enabling the lithium metal electrode for high-energy and low-cost rechargeable batteries. *Nat. Energy* **3**, 16–21 (2018).
2. Li, C. *et al.* An advance review of solid-state battery: Challenges, progress and prospects. *Sustain. Mater. Technol.* **29**, e00297 (2021).
3. Arbizzani, C., Gabrielli, G. & Mastragostino, M. Thermal stability and flammability of electrolytes for lithium-ion batteries. *J. Power Sources* **196**, 4801–4805 (2011).
4. Al-Salih, H., Houache, M. S. E., Baranova, E. A. & Abu-Lebdeh, Y. Composite Cathodes for Solid-State Lithium Batteries: "Catholytes" the Underrated Giants. *Adv. Energy Sustain. Res.* **3**, 2200032 (2022).
5. Neumann, A. *et al.* Analysis of Interfacial Effects in All-Solid-State Batteries with Thiophosphate Solid Electrolytes. *ACS Appl. Mater. Interfaces* **12**, 9277–9291 (2020).
6. Oh, Y. S., Kim, M., Kang, S., Park, J.-Y. & Lim, H.-T. Redox activity of Li_2S–P_2S_5 electrolyte inducing chemo-mechanical failure in all-solid-state batteries comprising sulfur composite cathode and Li–Si alloy anode. *Chem. Eng. J.* **442**, 136229 (2022).
7. Tsukasaki, H. *et al.* Analysis of structural and thermal stability in the positive electrode for sulfide-based all-solid-state lithium batteries. *J. Power Sources* **367**, 42–48 (2017).
8. Strauss, F. *et al.* Influence of electronically conductive additives on the cycling performance of argyrodite-based all-solid-state batteries. *RSC Adv.* **10**, 1114–1119 (2020).
9. Kim, A.-Y. *et al.* Stabilizing Effect of a Hybrid Surface Coating on a Ni-Rich NCM Cathode Material in All-Solid-State Batteries. *Chem. Mater.* **31**, 9664–9672 (2019).

10. Liang, J. *et al.* In Situ Li_3PS_4 Solid-State Electrolyte Protection Layers for Superior Long-Life and High-Rate Lithium-Metal Anodes. *Adv. Mater.* **30**, 1804684 (2018).
11. Walther, F. *et al.* The Working Principle of a $Li_2CO_3/LiNbO_3$ Coating on NCM for Thiophosphate-Based All-Solid-State Batteries. *Chem. Mater.* **33**, 2110–2125 (2021).
12. Payandeh, S., Strauss, F., Mazilkin, A., Kondrakov, A. & Brezesinski, T. Tailoring the $LiNbO_3$ coating of Ni-rich cathode materials for stable and high-performance all-solid-state batteries. *Nano Res. Energy* **1**, e9120016 (2022).
13. Liang, J. *et al.* A gradient oxy-thiophosphate-coated Ni-rich layered oxide cathode for stable all-solid-state Li-ion batteries. *Nat. Commun.* **14**, 146 (2023).
14. Jiang, H. *et al.* Insights into interfacial chemistry of Ni-rich cathodes and sulphide-based electrolytes in all-solid-state lithium batteries. *Chem. Commun.* **58**, 5924–5947 (2022).
15. Xin, F. *et al.* Electrochemical Characterization and Microstructure Evolution of Ni-Rich Layered Cathode Materials by Niobium Coating/Substitution. *Chem. Mater.* **34**, 7858–7866 (2022).
16. Xin, F. *et al.* Li–Nb–O Coating/Substitution Enhances the Electrochemical Performance of the $LiNi_{0.8}Mn_{0.1}Co_{0.1}O_2$ (NMC 811) Cathode. *ACS Appl. Mater. Interfaces* **11**, 34889–34894 (2019).
17. Aiken, C. P. *et al.* A Survey of In Situ Gas Evolution during High Voltage Formation in Li-Ion Pouch Cells. *J. Electrochem. Soc.* **162**, A760 (2015).
18. Doerrer, C. *et al.* High Energy Density Single-Crystal NMC/Li_6PS_5Cl Cathodes for All-Solid-State Lithium-Metal Batteries. *ACS Appl. Mater. Interfaces* **13**, 37809–37815 (2021).

19. Kim, S. Y., Cha, H., Kostecki, R. & Chen, G. Composite Cathode Design for High-Energy All-Solid-State Lithium Batteries with Long Cycle Life. *ACS Energy Lett.* **8**, 521–528 (2023).

20. Strauss, F. *et al.* Impact of Cathode Material Particle Size on the Capacity of Bulk-Type All-Solid-State Batteries. *ACS Energy Lett.* **3**, 992–996 (2018).

21. Shi, T. *et al.* Characterization of mechanical degradation in an all-solid-state battery cathode. *J. Mater. Chem. A* **8**, 17399–17404 (2020).

22. Kroll, M. *et al.* Sheet-type all-solid-state batteries with sulfidic electrolytes: Analysis of kinetic limitations based on a cathode morphology study. *J. Power Sources* **505**, 230064 (2021).

23. Liu, Y., Hamam, I. & Dahn, J. R. A Study of Vinylene Carbonate and Prop-1-ene-1,3 Sultone Electrolyte Additives Using Polycrystalline $Li[Ni_{0.6}Mn_{0.2}Co_{0.2}]O_2$ in Positive/Positive Symmetric Cells. *J. Electrochem. Soc.* **167**, 110527 (2020).

24. Märker, K., Reeves, P. J., Xu, C., Griffith, K. J. & Grey, C. P. Evolution of Structure and Lithium Dynamics in $LiNi_{0.8}Mn_{0.1}Co_{0.1}O_2$ (NMC811) Cathodes during Electrochemical Cycling. *Chem. Mater.* **31**, 2545–2554 (2019).

25. Ryu, H.-H., Park, K.-J., Yoon, C. S. & Sun, Y.-K. Capacity Fading of Ni-Rich $Li[Ni_xCo_yMn_{1-x-y}]O_2$ ($0.6 \le x \le 0.95$) Cathodes for High-Energy-Density Lithium-Ion Batteries: Bulk or Surface Degradation? *Chem. Mater.* **30**, 1155–1163 (2018).

26. Cadiou, F., Nguyen, T.T., Bettge, M., Su, Z., Ando, J., De Andrade, V., Miller, D., Demortière, A. Morphological Evolution of NMC Secondary Particles Through in situ

electrochemical FIB/SEM experiment. ArXiv (Chemical Physics), Submitted on 1 Aug. 2022, https://doi.org/10.48550/arXiv.2208.00878, (Accessed 2022-10-18)

27. Song, B. *et al.* Nano-structural changes in Li-ion battery cathodes during cycling revealed by FIB-SEM serial sectioning tomography. *J. Mater. Chem. A* **3**, 18171–18179 (2015).
28. Ruess, R. *et al.* Influence of NCM Particle Cracking on Kinetics of Lithium-Ion Batteries with Liquid or Solid Electrolyte. *J. Electrochem. Soc.* **167**, 100532 (2020).
29. Sakuda, A., Hayashi, A. & Tatsumisago, M. Sulfide Solid Electrolyte with Favorable Mechanical Property for All-Solid-State Lithium Battery. *Sci. Rep.* **3**, 2261 (2013).
30. McGrogan, F. P. *et al.* Compliant Yet Brittle Mechanical Behavior of Li_2S–P_2S_5 Lithium-Ion-Conducting Solid Electrolyte. *Adv. Energy Mater.* **7**, 1602011 (2017).
31. Athanasiou, C. E. *et al.* Rate-dependent deformation of amorphous sulfide glass electrolytes for solid-state batteries. *Cell Rep. Phys. Sci.* **3**, 100845 (2022).
32. Hikima, K., Totani, M., Obokata, S., Muto, H. & Matsuda, A. Mechanical Properties of Sulfide-Type Solid Electrolytes Analyzed by Indentation Methods. *ACS Appl. Energy Mater.* **5**, 2349–2355 (2022).
33. Hänsel, C. & Kundu, D. The Stack Pressure Dilemma in Sulfide Electrolyte Based Li Metal Solid-State Batteries: A Case Study with Li_6PS_5Cl Solid Electrolyte. *Adv. Mater. Interfaces* **8**, 2100206 (2021).
34. Kodama, M., Ohashi, A. & Hirai, S. In situ X-ray computational tomography measurement of single particle behavior of sulfide solid electrolyte under high-pressure compression. *J. Power Sources Adv.* **4**, 100019 (2020).

35. Peng, J. *et al.* High-safety, wide-temperature-range, low-external-pressure and dendrite-free lithium battery with sulfide solid electrolyte. *Energy Storage Mater.* **54**, 430–439 (2023).

36. Cheng, E. J. *et al.* Mechanical and physical properties of $LiNi_{0.33}Mn_{0.33}Co_{0.33}O_2$ (NMC). *J. Eur. Ceram. Soc.* **37**, 3213–3217 (2017).

37. Perrenot, P. *et al.* Room temperature sintering of amorphous thiophosphates solid electrolyte (Li_3PS_4): coupling morphological evolution to electrochemical properties. *Advanced Functional Materials,* 2310739 (2023).

38. Walther, F. *et al.* Influence of Carbon Additives on the Decomposition Pathways in Cathodes of Lithium Thiophosphate-Based All-Solid-State Batteries. *Chem. Mater.* **32**, 6123–6136 (2020).

39. Yoon, K., Kim, J.-J., Seong, W. M., Lee, M. H. & Kang, K. Investigation on the interface between $Li_{10}GeP_2S_{12}$ electrolyte and carbon conductive agents in all-solid-state lithium battery. *Sci. Rep.* **8**, 8066 (2018).

40. Zhang, W. *et al.* The Detrimental Effects of Carbon Additives in $Li_{10}GeP_2S_{12}$-Based Solid-State Batteries. *ACS Appl. Mater. Interfaces* **9**, 35888–35896 (2017).

41. Wu, X. Operando characterization of degradation phenomena in all-solid-state batteries with a sulfide-based solid electrolyte. (ETH Zurich, 2019). doi:10.3929/ethz-b-000352747.

42. Wu, X. *et al.* Operando Visualization of Morphological Dynamics in All-Solid-State Batteries. *Adv. Energy Mater.* **9**, 1901547 (2019).

43. Tsai, E. H. R. *et al.* Correlated X-Ray 3D Ptychography and Diffraction Microscopy Visualize Links between Morphology and Crystal Structure of Lithium-Rich Cathode Materials. *iScience* **11**, 356–365 (2019).